Energy Materials

Supplementary Materials

Trace Mn doping activates ZIF-67 through reconstruction to Co-Mn (Oxy)hydroxides for enhanced oxygen evolution

Deyou Liu[1,2], Hanwen Luan[3], Hongjie Guo[1], Yongqiang Li[2], Ningning Shao[2], Roberto Boada[3], Zhijun Dong[2], Hongliang Li[1,*], Xiang-Yang Lou[2,*], Zhijie Chen[4]

[1]College of Mining Engineering, Taiyuan University of Technology, Taiyuan 030024, Shanxi, China.
[2]Institute of Technology for Future Industry (School of Science and Technology Instrument Application Engineering), Shenzhen University of Information Technology, Shenzhen 518172, Guangdong, China.
[3]GTS-UAB Research Group, Department of Chemistry, Facultat de Ciències, Universitat Autònoma de Barcelona, Bellaterra 08193, Spain.
[4]UNSW Water Research Centre, School of Civil and Environmental Engineering, University of New South Wales, Sydney 2052, Australia.

Correspondence to: Prof. Hongliang Li, College of Mining Engineering, Taiyuan University of Technology, Taiyuan 030024 Shanxi, China. E-mail: lihongliang222@126.com; Prof. Xiang-Yang Lou, Institute of Technology for Future Industry (School of Science and Technology Instrument Application Engineering), Shenzhen University of Information Technology, Shenzhen 518172, Guangdong, China. E-mail: louxiangyang@sziit.edu.cn

Supplementary Figure 4. Nitrogen adsorption-desorption isotherms of ZIF-67 and Mn-ZIF-67 measured at 77 K.

Supplementary Figure 5. BJH adsorption pore-size distributions of ZIF-67 and Mn-ZIF-67.

Supplementary Figure 6. LSV backscan curve of Mn-ZIF-67 after electrochemical activation in 1.0 M KOH.

Supplementary Figure 7. Chronopotentiometry curve of Mn-ZIF-67/NF at 1 A cm^{-2} in 1.0 M KOH for 24 h.

Supplementary Figure 8. Equivalent circuit model for EIS data fitting.

Supplementary Figure 9. CV measurements of ZIF-67 at different scan rates for C_{dl} determination.

Supplementary Figure 10. CV measurements of NF at different scan rates for C_{dl} determination.

Supplementary Figure 11. XRD patterns of Mn-ZIF-67 before and after OER.

Supplementary Figure 12. Co 2p XPS spectrum of ZIF-67 after the OER.

Supplementary Figure 13. HRTEM image of ZIF-67 after the OER.

Supplementary Figure 14. XRD patterns of as-prepared Mn-ZIF-67 and Mn-ZIF-67 after alkaline seawater electrolysis.

Supplementary Figure 15. Co 2p XPS spectrum of Mn-ZIF-67 after alkaline seawater electrolysis.

Supplementary Figure 16. Mn 2p XPS spectrum of Mn-ZIF-67 after alkaline seawater electrolysis.

Supplementary Table 1. Major-ion concentrations in natural seawater collected from Shenzhen Bay before KOH addition.

Supplementary Table 2. Textural parameters of ZIF-67 and Mn-ZIF-67 derived from nitrogen adsorption-desorption measurements.

Supplementary Table 3. Calculated charge transfer resistance (R_f, R_{ct}) and solution resistance (R_s) of the materials deposited on NF obtained from EIS experiments.

Supplementary Table 4. Comparison of apparent OER performance and electrochemical surface descriptors of Mn-ZIF-67 with representative ZIF-67/MOF-based and transition-metal electrocatalysts.

Supplementary Table 5. ICP analysis of Mn and Co contents before and after long-term OER operation.

Supplementary Note 1. Chemicals and reagents

Cobalt(II) nitrate hexahydrate ($Co(NO_3)_2 \cdot 6H_2O$, ≥ 99.0%), manganese(II) nitrate tetrahydrate ($Mn(NO_3)_2 \cdot 4H_2O$, ≥ 98.0%), and 2-methylimidazole (2-MIM, 99%) were purchased from Shanghai Macklin Biochemical Co., Ltd. Methanol (CH_3OH, analytical reagent) and potassium hydroxide (KOH, analytical reagent) were obtained from Sinopharm Chemical Reagent Co., Ltd. Natural seawater was collected from Shenzhen Bay (Shenzhen, China) for the preparation of the alkaline seawater electrolyte. All chemical reagents were used as received without further purification. Deionized (DI) water (18.2 MΩ cm) was used throughout all experiments.

Supplementary Note 2. Physicochemical characterization

The crystal structures of the samples were characterized using a Bruker D8 Advance X-ray diffractometer (XRD) equipped with a Cu Kα radiation source. The diffractometer was operated at a voltage of 40 kV and a current of 40 mA, and diffraction patterns were collected over a 2θ range of 10-80° at a scan rate of 10° min^{-1}. The surface morphology of the samples was examined using a Zeiss Gemini 300 field emission scanning electron microscope (SEM), while the elemental distribution was determined using an attached energy-dispersive X-ray spectrometer (EDS) detector. Transmission electron microscopy (TEM) observations were conducted on an FEI Talos 200X microscope operated at an accelerating voltage of 200 kV to investigate the nanoscale structure features. High-resolution TEM (HRTEM) images and selected area electron diffraction (SAED) patterns were further acquired to elucidate the detailed microstructure and crystallinity of the samples. X-ray photoelectron spectroscopy (XPS) measurements were performed on a Thermo Fisher ESCALAB Xi+ spectrometer using an Al Kα X-ray source to analyze the surface elemental composition and chemical states. High-resolution spectra were collected for the Co 2p, Mn 2p, N 1s, C 1s, and O 1s regions. All binding energies were calibrated using the adventitious C 1s peak at 284.8 eV as the reference. Nitrogen adsorption-desorption isotherms were measured at 77 K on a Micromeritics ASAP 2460 surface area and porosity analyzer. Prior to measurement, the samples were degassed under vacuum at 120 °C for 12 h. Specific surface areas were calculated using the Brunauer-Emmett-Teller (BET) method over the relative pressure range P/P0 = 0.05-0.30, micropore area and volume were derived from the t-plot method, and pore-size distributions were obtained from the Barrett-Joyner-Halenda (BJH) model applied to

the adsorption branch. In-situ electrochemical Raman spectra were collected in 1.0 M KOH using an electrochemical Raman cell. A 633 nm laser was used as the excitation source. The catalyst-modified electrode was used as the working electrode, with a graphite rod as the counter electrode and Hg/HgO as the reference electrode. Raman spectra were recorded at different applied potentials from OCP to 1.80 V to monitor the potential-dependent surface reconstruction during OER. All applied potentials were converted to the RHE scale.

Supplementary Note 3. Collection and preparation of the alkaline seawater electrolyte

Regarding the overall alkaline seawater splitting, the electrolyte used was prepared based on natural seawater. The natural seawater was collected from Shenzhen Bay in Shenzhen, Guangdong province, China. Prior to electrochemical testing, the collected seawater was carefully filtered through a 0.22 μm membrane filter to remove insoluble solid impurities, suspended particles, and marine microorganisms. Subsequently, commercial potassium hydroxide (KOH) was dissolved into the filtered seawater to achieve a concentration of 1.0 M. This formulated 1.0 M KOH seawater was directly utilized as the alkaline seawater electrolyte for all related overall water splitting tests without further purification. No softening or removal of hard cations (Ca^{2+} and Mg^{2+}) was performed prior to the addition of KOH, so that the electrolyte retains the native ionic composition of the collected seawater.

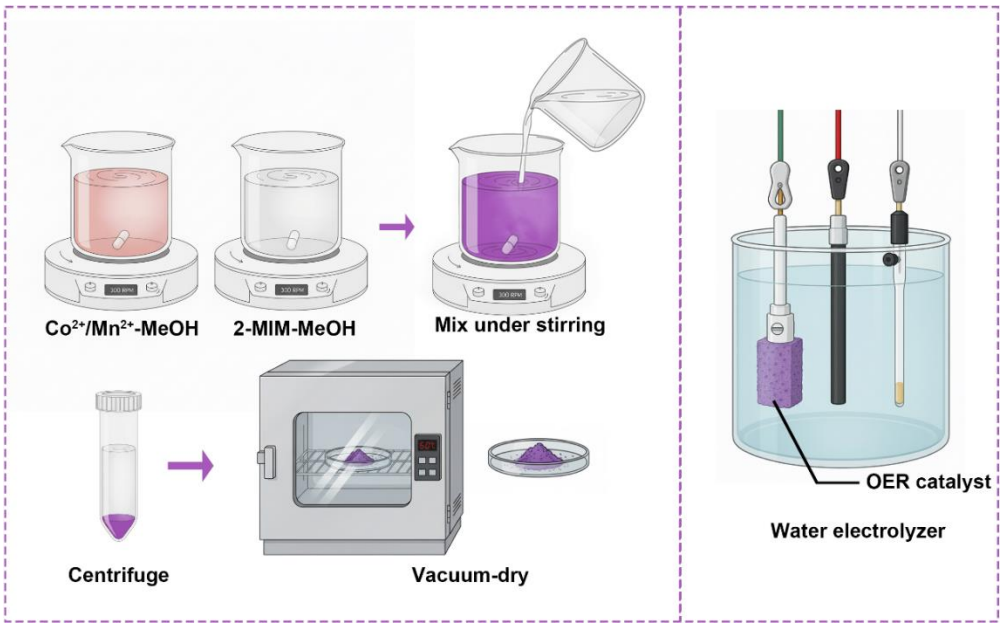

Supplementary Figure 1. Schematic illustration of (left) the room-temperature synthesis procedure for the Mn-ZIF-67 catalyst, involving solution mixing, centrifugation, and vacuum-drying, and (right) the three-electrode system setup for OER performance measurements.

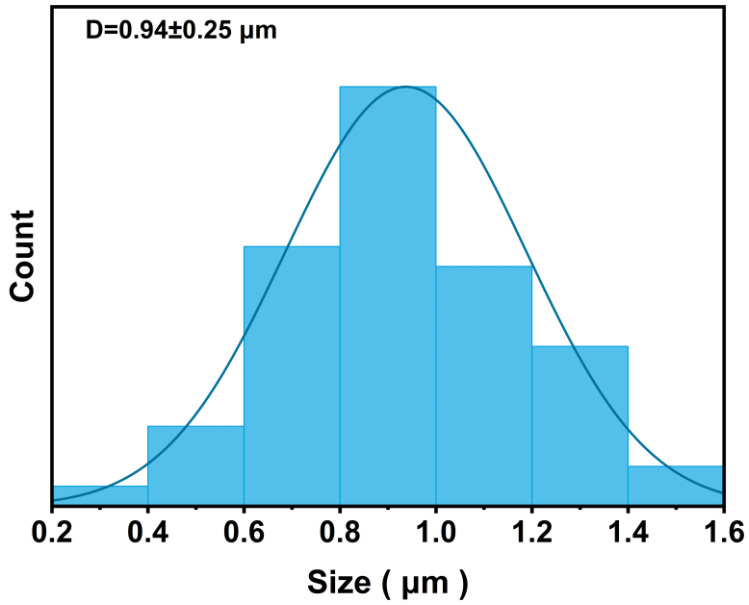

Supplementary Figure 2. Particle size distribution histograms for ZIF-67. The data were statistically derived from SEM images shown in Figure 1A.

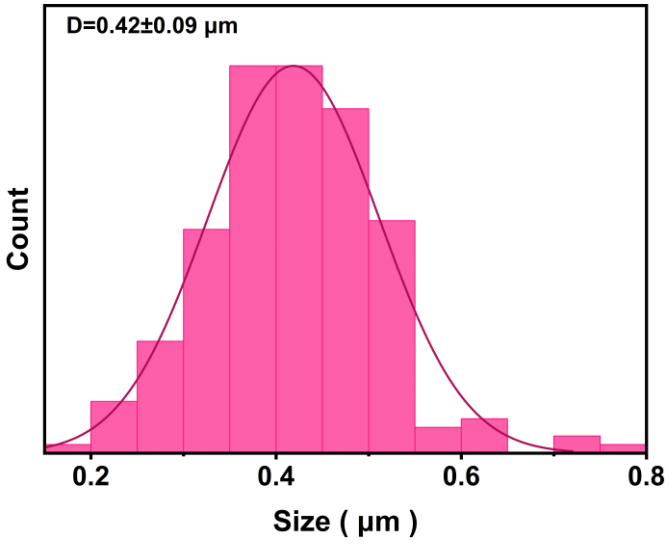

Supplementary Figure 3. Particle size distribution histograms for Mn-ZIF-67. The data were statistically derived from SEM images shown in Figure 1B.

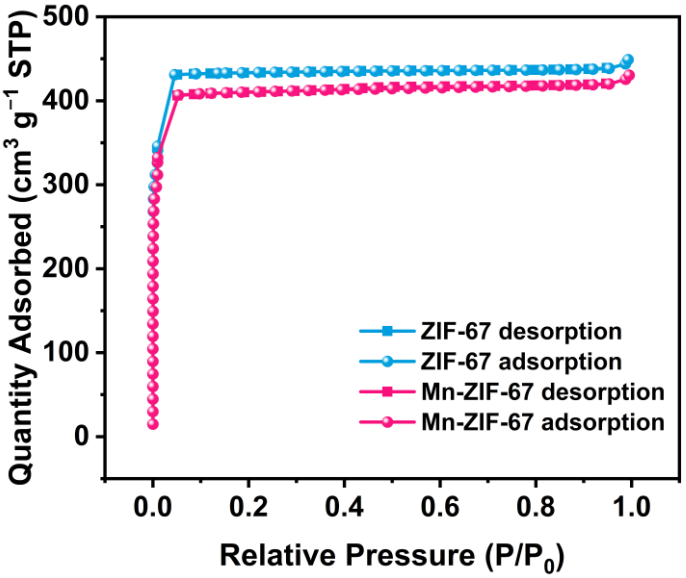

Supplementary Figure 4. Nitrogen adsorption-desorption isotherms of ZIF-67 and Mn-ZIF-67 measured at 77 K.

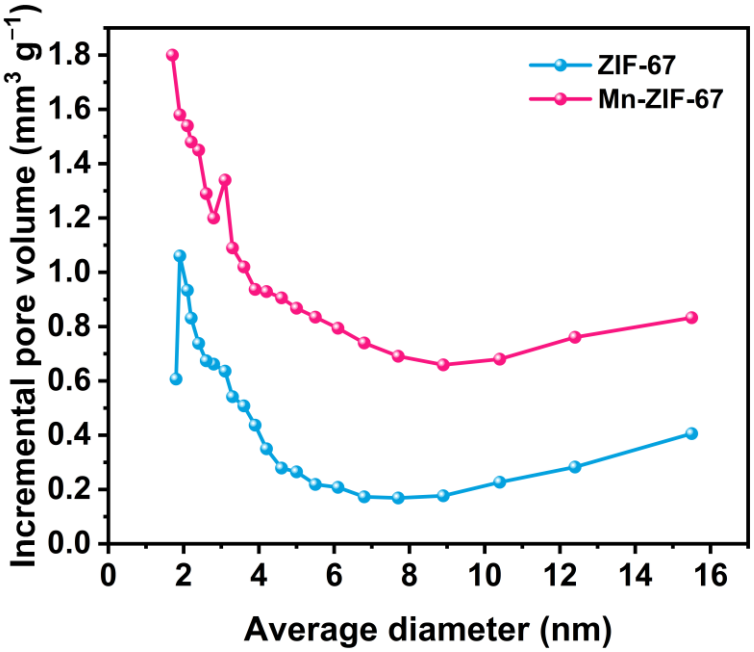

Supplementary Figure 5. BJH adsorption pore-size distributions of ZIF-67 and Mn-ZIF-67.

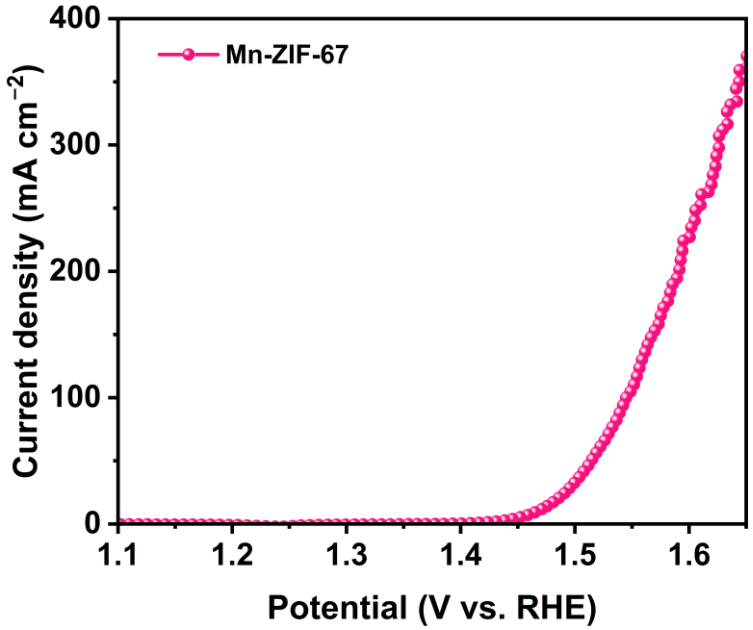

Supplementary Figure 6. LSV backscan curve of Mn-ZIF-67 after electrochemical activation in 1.0 M KOH. The backscan measurement was performed to minimize the possible influence of Ni foam oxidation on the evaluation of OER activity in the low-current-density region.

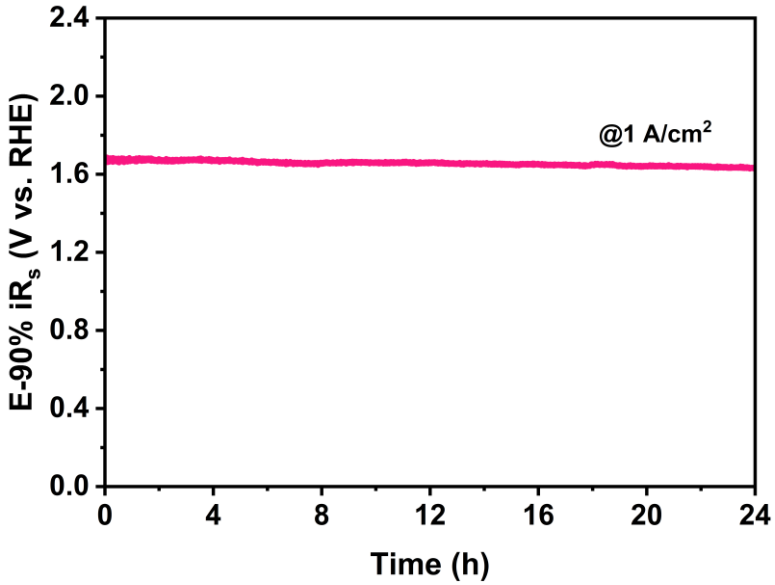

Supplementary Figure 7. Chronopotentiometry curve of Mn-ZIF-67/NF at 1 A cm^{-2} in 1.0 M KOH for 24 h, measured in a three-electrode configuration with 90% iR compensation.

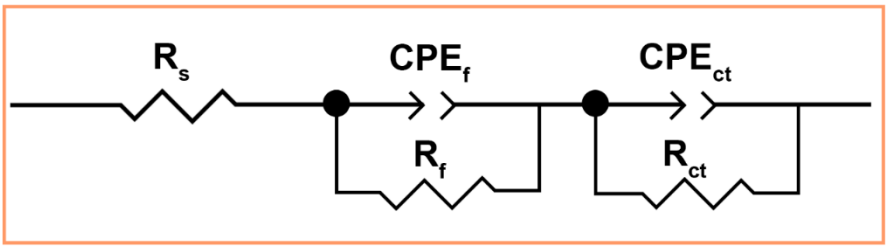

Supplementary Figure 8. Equivalent circuit model for EIS data fitting.

In this equivalent circuit, R_s represents the electrolyte resistance, R_f represents the catalyst film resistance related to the porous catalyst layer and catalyst/NF interface, and R_{ct} represents the Faradaic charge-transfer resistance associated with the OER process. The R_f/CPE_f component describes the dielectric and resistive response of the catalyst film/interface, while the R_{ct}/CPE_{ct} component corresponds to the OER charge-transfer process at the catalyst/electrolyte interface. Therefore, the introduction of R_f is necessary to distinguish the catalyst-film/interface contribution from the OER charge-transfer resistance.

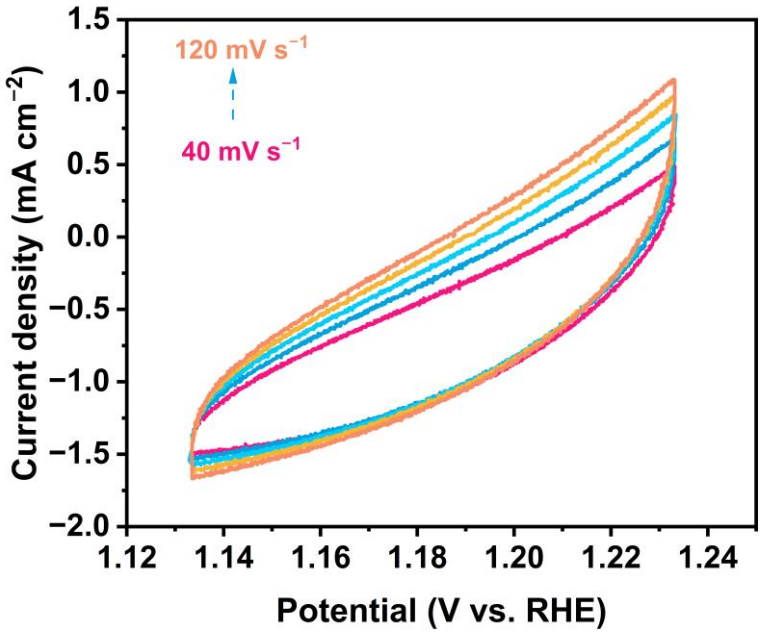

Supplementary Figure 9. CV measurements of ZIF-67 at different scan rates for C_{dl} determination.

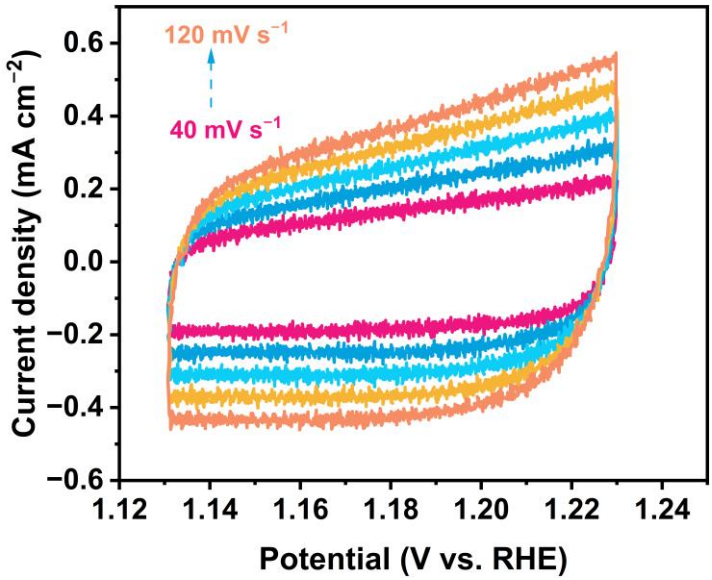

Supplementary Figure 10. CV measurements of NF at different scan rates for C_{dl} determination.

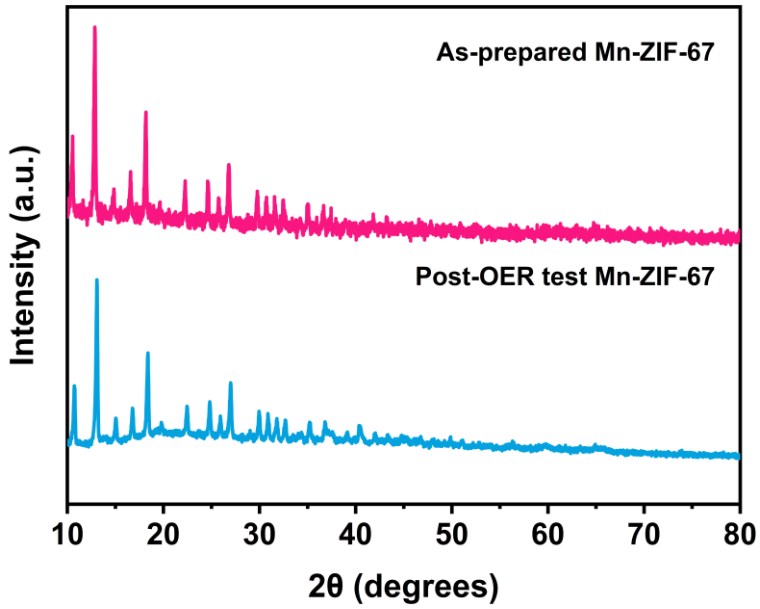

Supplementary Figure 11. XRD patterns of Mn-ZIF-67 before and after OER.

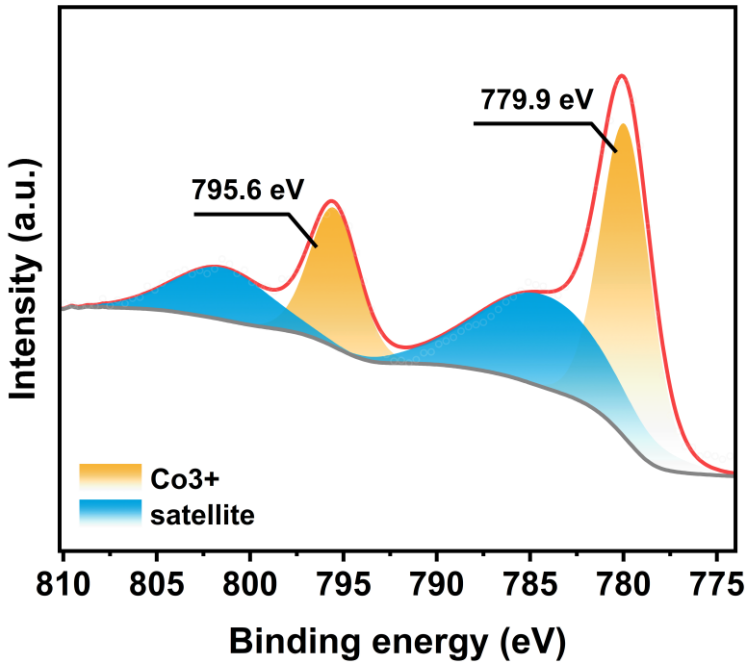

Supplementary Figure 12. High-resolution Co 2p XPS spectrum of ZIF-67 after the OER in 1.0 M KOH. The Co $2p_{3/2}$ and Co $2p_{1/2}$ peaks at 779.9 and 795.6 eV are assigned to Co^{3+} species, and the pronounced satellite features indicate incomplete surface oxidation.

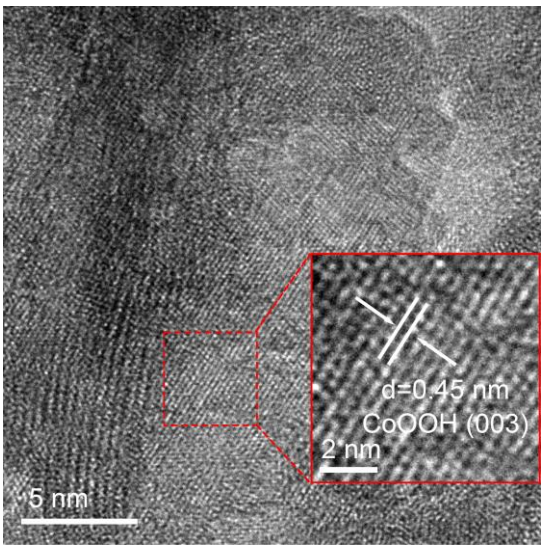

Supplementary Figure 13. HRTEM image of ZIF-67 after the OER in 1.0 M KOH. The lattice fringes with an interplanar spacing of 0.45 nm correspond to the CoOOH (003) plane, confirming that pristine ZIF-67 also undergoes electrochemical reconstruction into CoOOH-like species during the OER.

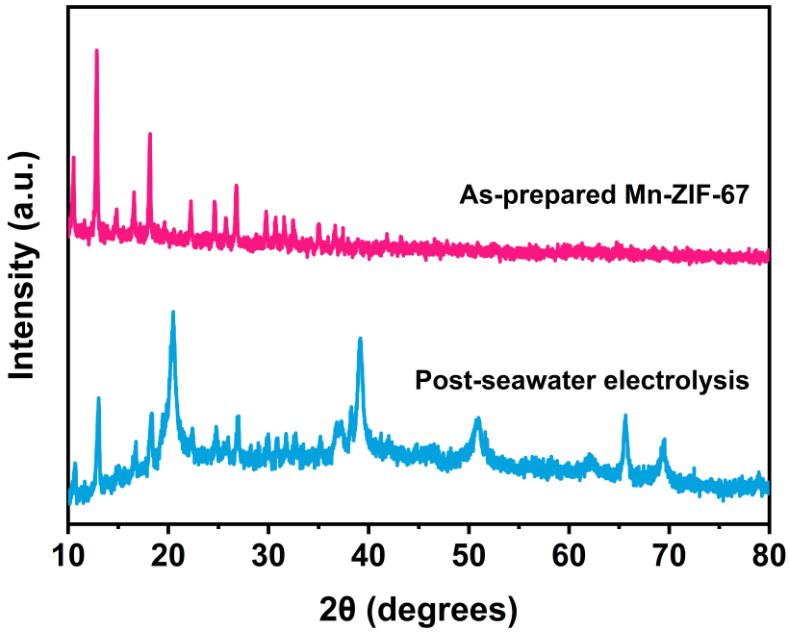

Supplementary Figure 14. XRD patterns of as-prepared Mn-ZIF-67 and Mn-ZIF-67 after alkaline seawater electrolysis. No obvious crystalline chloride-containing corrosion products are detected after seawater electrolysis.

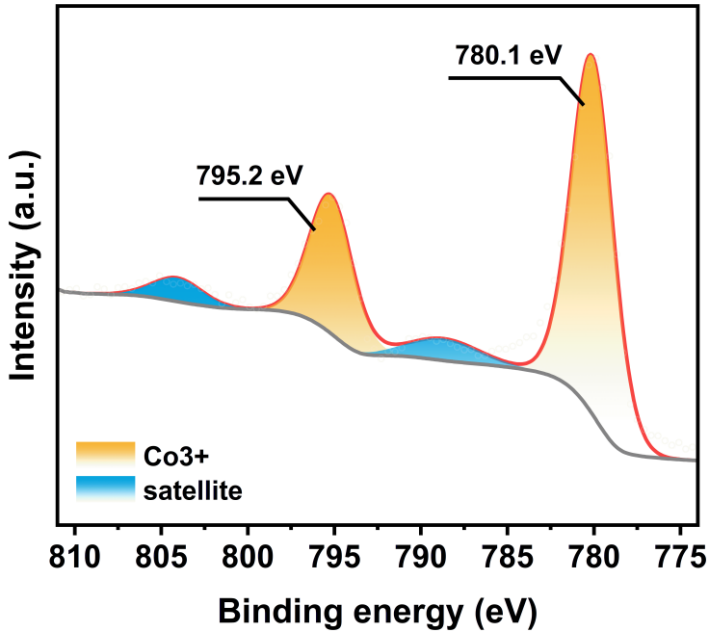

Supplementary Figure 15. High-resolution Co 2p XPS spectrum of Mn-ZIF-67 after alkaline seawater electrolysis. The Co $2p_{3/2}$ and Co $2p_{1/2}$ peaks at 780.1 and 795.2 eV with weak satellite features indicate that the Co^{3+}-dominated oxyhydroxide-like surface is well preserved.

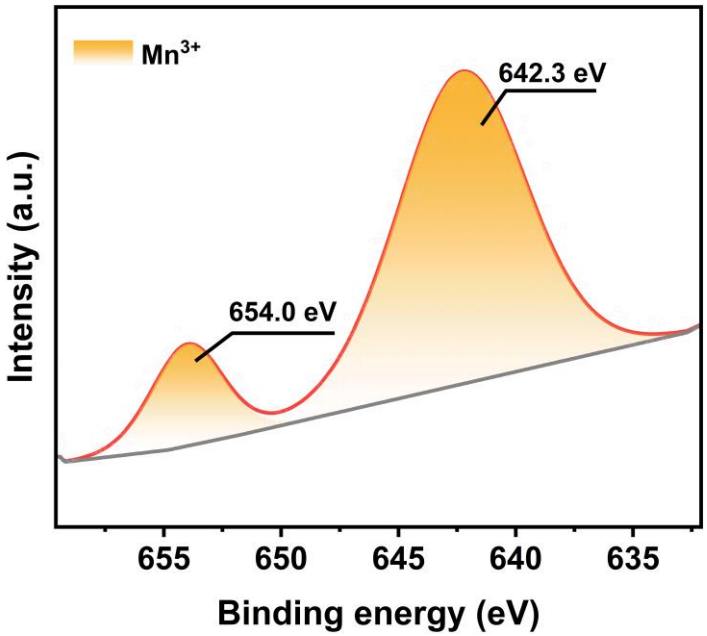

Supplementary Figure 16. High-resolution Mn 2p XPS spectrum of Mn-ZIF-67 after alkaline seawater electrolysis. The Mn $2p_{3/2}$ and Mn $2p_{1/2}$ peaks at 642.3 and 654.0 eV are consistent with Mn^{3+} oxyhydroxide-like species, confirming that Mn is retained in the reconstructed Co-Mn (oxy)hydroxide layer.

Supplementary Table 1. Major-ion concentrations in natural seawater collected from Shenzhen Bay before KOH addition[1]

Ion	Concentration (mg L^{-1})
Na^+	11,159
Mg^{2+}	1,292
Ca^{2+}	516
K^+	292
Cl^-	17,535
SO_4^{2-}	2,588
Br^-	68

Supplementary Table 2. Textural parameters of ZIF-67 and Mn-ZIF-67 derived from nitrogen adsorption-desorption measurements

Textural parameter	ZIF-67	Mn-ZIF-67
BET surface area (m^2 g^{-1})	1264.18	1238.33
Langmuir surface area (m^2 g^{-1})	1903.93	1820.15

t-plot micropore area ($m^2 g^{-1}$)	1240.68	1197.37
t-plot external surface area ($m^2 g^{-1}$)	23.50	40.97
Total pore volume ($cm^3 g^{-1}$)	0.6945	0.6657
t-plot micropore volume ($cm^3 g^{-1}$)	0.6602	0.6168
BJH adsorption cumulative area ($m^2 g^{-1}$)	15.49	30.96
BJH adsorption cumulative volume ($cm^3 g^{-1}$)	0.03025	0.04332

Note: The BET data indicate that Mn-ZIF-67 has a slightly lower total BET surface area but a higher external surface area and larger BJH-derived pore contribution.

Supplementary Table 3. Calculated catalyst film resistance (R_f, R_{ct}) and solution resistance (R_s) (in Ohm, Ω) of the materials deposited on NF obtained from the Nyquist plot during the EIS experiments

	R_s	R_f	R_{ct}
Mn-ZIF-67	0.80	0.18	2.17
ZIF-67	0.83	0.22	4.60
NF	0.87	9.76	35.36

Supplementary Table 4. Comparison of apparent OER performance and electrochemical surface descriptors of Mn-ZIF-67 with representative ZIF-67/MOF-based and transition-metal electrocatalysts

No.	Catalyst	Electrolyte	Overpotential	Tafel slope ($mV\ dec^{-1}$)	ECSA	Reference
1	Mn-ZIF-67 (this work)	1.0 M KOH	235 mV (10 mA cm^{-2}); 310 mV (100 mA cm^{-2})	36.49	120.50 cm^2	This work
2	ZIF-67 (this work)	1.0 M KOH	276 mV (10 mA cm^{-2}); 353 mV (100 mA cm^{-2})	50.12	63.25 cm^2	This work
3	GO@ZIF-67@MnFe	1.0 M KOH	236 mV (10 mA cm^{-2})	55.7	C_{dl} = 123 mF cm^{-2}	[2]

4	ZIF-67@CNT	alkaline water electrolysis	285 mV (10 mA cm^{-2})	57	-	[3]
5	CoO_x-ZIF	1.0 M KOH	318 mV (10 mA cm^{-2})	70.3	112.59 cm^2	[4]
6	FeNiO NP@ZnCo ZIF	0.1 M NaOH	460 mV (10 mA cm^{-2})	82	C_{dl} = 255 μF cm^{-2}	[5]
7	ZIF-L@Fe28	1.0 M KOH	312 mV (10 mA cm^{-2})	78	472.5 m^2 g^{-1}	[6]
8	Yolk/shell ZIF-67@POM	1.0 M KOH	287 mV (10 mA cm^{-2})	58	-	[7]
9	ZIF-8@ZIF-67@POM	1.0 M KOH	490 mV (10 mA cm^{-2})	88	-	[8]
10	PBA@POM	1.0 M KOH	440 mV (10 mA cm^{-2})	23	-	[9]
11	SiW_9Co_3@ ZIF-67	0.1 M KOH	420 mV (10 mA cm^{-2})	94	-	[10]
12	Mo_xCoxC @C	1.0 M KOH	295 mV (10 mA cm^{-2})	39	-	[11]
13	Fe/Ni2.4/Co0.4-MIL-53	1.0 M KOH	219 mV (10 mA cm^{-2})	54	-	[12]
14	Quasi-ZIF-67-350	1.0 M KOH	286 mV (10 mA cm^{-2})	84	-	[13]
15	$WS_2/Co_{1-x}S$/N	1.0 M KOH	365 mV (10 mA cm^{-2})	64	-	[14]
16	Co_3O_4/Co MoO_4 nanocages	1.0 M KOH	318 mV (10 mA cm^{-2})	63	-	[15]
17	NiFe-	1.0 M KOH	217 mV (100	-	285	[16]

BDC@ZIF-67	mA cm^{-2})	cm^2

Supplementary Table 5. ICP analysis of Mn and Co contents before and after long-term OER operation

Sample	Mn / wt%	Co / wt%	Mn/Co atomic ratio	Mn retention ratio
Before OER	2.5389 ± 0.0301	27.10 ± 0.40	0.10051 ± 0.00241	100%
After long-term OER	2.6528 ± 0.0467	31.58 ± 0.27	0.09014 ± 0.00235	89.7%

Note: Values are presented as mean ± standard deviation based on three parallel ICP measurements (n = 3). The Mn retention ratio was calculated from the normalized Mn/Co atomic ratios before and after long-term OER operation.

REFERENCES

1. X. Gu, X. Feng, S. Yang, R. Wang, Q. Zeng, Y. Shangguan, J. Liang, H. Zhou, Z. Li, Z. Lin, C. Zheng, Z. Xu, H. Chen, Photovoltaic-driven dual-oxidation seawater electrolyzer for sustainable lithium recovery, *Proc. Natl. Acad. Sci.* 121 (2024) e2414741121. DOI: 10.1073/pnas.2414741121.

2. Z. Naghshbandi, K. Moradi, A. Salimi, M. Gholinejad, A. Feizabadi, Multi metallic electro-catalyst design for enhanced oxygen evolution reaction: immobilizing MnFe nanoparticles on ZIF-67-decorated graphene oxide, *Electrochim. Acta* 479 (2024) 143884. DOI: 10.1016/j.electacta.2024.143884.

3. H.B. Jung, Y. Kim, J. Lim, S. Cho, M. Seo, I.-S. Kim, M. Kim, C. Lee, Y.-W. Lee, C.-Y. Yoo, Y. Oh, J. Hong, H.-S. Cho, Y. Cho, ZIF-67 metal-organic frameworks synthesized onto CNT supports for oxygen evolution reaction in alkaline water electrolysis, *Electrochim. Acta* 439 (2023) 141593. DOI: 10.1016/j.electacta.2022.141593.

4. S. Dou, C.-L. Dong, Z. Hu, Y.-C. Huang, J. Chen, L. Tao, D. Yan, D. Chen, S. Shen, S. Chou, S. Wang, Atomic-scale CoO_x species in metal–organic frameworks for oxygen evolution reaction, *Adv. Funct. Mater.* 27 (2017) 1702546. DOI: 10.1002/adfm.201702546.

5. S. Ghoshal, S. Zaccarine, G.C. Anderson, M.B. Martinez, K.E. Hurst, S. Pylypenko, B.S. Pivovar, S.M. Alia, ZIF 67 based highly active electrocatalysts as oxygen electrodes in water electrolyzer, *ACS Appl. Energy Mater.* 2 (2019) 5568–5576. DOI: 10.1021/acsaem.9b00733.

6. Z. Xiao, F. Xu, A two-dimensional zeolitic imidazolate framework loaded with an acrylate-substituted oxoiron cluster as an efficient electrocatalyst for the oxygen evolution reaction, *New J. Chem.* 46 (2022) 11095–11100. DOI: 10.1039/D2NJ01771G.

7. Q.Y. Li, L. Zhang, Y.X. Xu, Q. Li, H. Xue, H. Pang, Smart yolk/shell ZIF-67@POM hybrids as efficient electrocatalysts for the oxygen evolution reaction, *ACS Sustainable Chem. Eng.* 7 (2019) 5027–5033. DOI: 10.1021/acssuschemeng.8b05744.

8. Y. Wang, Y. Wang, L. Zhang, C.-S. Liu, H. Pang, Core–shell-type ZIF-8@ZIF-67@POM hybrids as efficient electrocatalysts for the oxygen evolution reaction, *Inorg. Chem. Front.* 6 (2019) 2514–2520. DOI: 10.1039/C9QI00798A.

9. Y. Wang, Y. Wang, L. Zhang, C.-S. Liu, H. Pang, PBA@POM hybrids as efficient electrocatalysts for the oxygen evolution reaction, *Chem. - Asian J.* 14 (2019) 2790–2795. DOI: 10.1002/asia.201900791.

10. V.K. Abdelkader-Fernández, D.M. Fernandes, S.S. Balula, L. Cunha-Silva, C. Freire, Advanced framework-modified POM@ZIF-67 nanocomposites as enhanced oxygen evolution reaction electrocatalysts, *J. Mater. Chem. A* 8 (2020) 13509–13521. DOI: 10.1039/D0TA03898A.

11. C. Chen, A. Wu, H. Yan, Y. Xiao, C. Tian, H. Fu, Trapping $PMo_{12}O_{40}^{3-}$ clusters into pre-synthesized ZIF-67 toward Mo_xCo_x C particles confined in uniform carbon polyhedrons for efficient overall water splitting, *Chem. Sci.* 9 (2018) 4746–4755. DOI: 10.1039/C8SC01454J.

12. F.-L. Li, Q. Shao, X. Huang, J.-P. Lang, Nanoscale trimetallic metal–organic frameworks enable efficient oxygen evolution electrocatalysis, *Angew. Chem. Int. Ed.* 57 (2018) 1888–1892. DOI: 10.1002/anie.201711376.

13. R. Zhu, J. Ding, J. Yang, H. Pang, Q. Xu, D. Zhang, P. Braunstein, Quasi-ZIF-67 for boosted oxygen evolution reaction catalytic activity via a low temperature calcination, *ACS Appl. Mater. Interfaces* 12 (2020) 25037–25041. DOI: 10.1021/acsami.0c05450.

14. Z. Huang, Z. Yang, M.Z. Hussain, B. Chen, Q. Jia, Y. Zhu, Y. Xia, Polyoxometallates@zeolitic-imidazolate-framework derived bimetallic tungsten-

cobalt sulfide/porous carbon nanocomposites as efficient bifunctional electrocatalysts for hydrogen and oxygen evolution, *Electrochim. Acta* 330 (2020) 135335. DOI: 10.1016/j.electacta.2019.135335.

15. L. Zhang, T. Mi, M.A. Ziaee, L. Liang, R. Wang, Hollow POM@MOF hybrid-derived porous Co_3O_4/$CoMoO_4$ nanocages for enhanced electrocatalytic water oxidation, *J. Mater. Chem.* A 6 (2018) 1639–1647. DOI: 10.1039/C7TA08683K.

16. Y. Lu, M. Murad, D. Guo, C. Pei, X. Yu, MOF-on-MOF NiFe-BDC@ZIF-67 heterostructure nanoarrays for chloride-suppressed oxygen evolution in alkaline seawater, *Chem. Commun.* 62 (2026) 7132–7135. DOI: 10.1039/D6CC00589F.